

RSC Advances



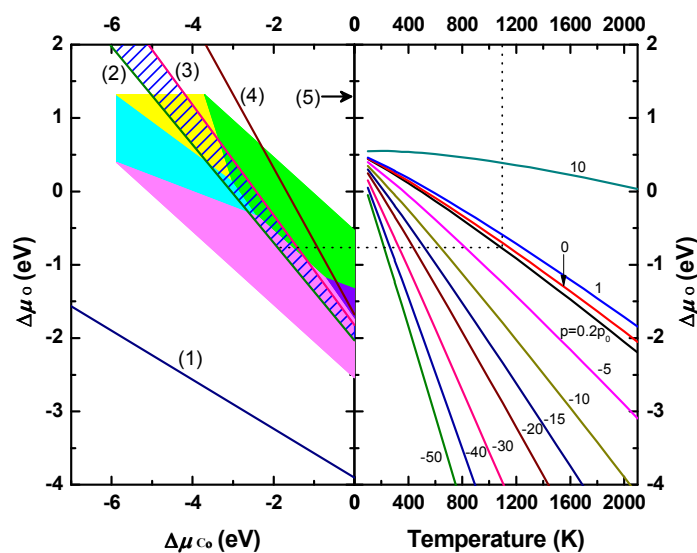
This is an *Accepted Manuscript*, which has been through the Royal Society of Chemistry peer review process and has been accepted for publication.

Accepted Manuscripts are published online shortly after acceptance, before technical editing, formatting and proof reading. Using this free service, authors can make their results available to the community, in citable form, before we publish the edited article. This *Accepted Manuscript* will be replaced by the edited, formatted and paginated article as soon as this is available.

You can find more information about *Accepted Manuscripts* in the [Information for Authors](#).

Please note that technical editing may introduce minor changes to the text and/or graphics, which may alter content. The journal's standard [Terms & Conditions](#) and the [Ethical guidelines](#) still apply. In no event shall the Royal Society of Chemistry be held responsible for any errors or omissions in this *Accepted Manuscript* or any consequences arising from the use of any information it contains.

Spin-polarized density functional theory calculations were used to investigate the atomic, electronic structures of ferromagnetic LaCoO_3 and $\text{La}_{1-x}\text{Sr}_x\text{CoO}_3$ surfaces. The thermodynamic stability of these surfaces was analyzed with phase diagrams drawn with the total energies obtained from calculations. The influence of Sr-doping was also examined.



Density functional theory calculations of atomic, electronic and thermodynamic properties of cubic LaCoO_3 and $\text{La}_{1-x}\text{Sr}_x\text{CoO}_3$ surfaces

Shuguang Zhang,^{*,†,‡} Ning Han,[†] Xiaoyao Tan[§]

[†] School of Chemical Engineering, Shandong University of Technology, Zibo 255049, China

[‡] Department of Chemical and Biomolecular Engineering, University of Notre Dame, Notre Dame 46556, USA

[§] Department of Chemical Engineering, Tianjin Polytechnic University, Tianjin 300387, China

*Corresponding author. E-mail: gregzhangsg@gmail.com

Abstract: Spin-polarized density functional theory calculations employing the generalized gradient approximation(GGA) +U scheme were used to investigate the atomic, electronic structures of ferromagnetic LaCoO_3 and $\text{La}_{1-x}\text{Sr}_x\text{CoO}_3$ surfaces. Nonstoichiometric symmetrical slab models were adopted. The thermodynamic stability of these surfaces was analyzed with phase diagrams drawn with the total energies obtained from calculations. The influence of Sr-doping on the thermodynamic stability of the surfaces was also examined. Results indicate that Sr ions prefer to substitute La ions in the outermost layers rather than those in bulk layers for both (001) surfaces. In undoped LaCoO_3 system, CoO_2 - and LaO -terminated (001) surfaces are the most stable two of all considered surfaces under typical operational conditions of the solid oxide fuel cells ($T = 1100$ K, $p\text{O}_2 = 0.2$ atm), while Sr-doping in LaCoO_3 crystal destabilizes the CoO_2 -terminated surface with respect to the $\text{La}_{0.75}\text{Sr}_{0.25}\text{O}$ -terminated surface.

Keywords: undoped and doped LaCoO_3 surfaces, thermodynamic stability, phase diagram analysis, GGA+ U calculation.

1. Introduction

Rational design of high active cathode materials for intermediate temperature solid oxide fuel cells (IT-SOFCs) remains one of the most critical scientific challenges.¹⁻⁴ To achieve this goal, however, it is urgent to reveal the intrinsic relationship between the surface catalytic properties and the chemical composition and structure of the cathode materials. Although various electrochemical² and *in situ* vibrational surface spectroscopy⁵ techniques have been applied to investigate cathode performance, the detailed mechanisms of surface oxygen reduction reaction (ORR) and bulk transport processes are still unclear due to the complexity of the interfaces. First-principles calculation may be a powerful approach to elucidate the oxygen-surfaces interaction nature through providing details about electronic structures, geometrical parameters, potential energy surface, transition states and intermediate species. Although Kotomin⁶⁻⁸ and M. L. Liu^{9,10} had used it to study the ORR mechanisms at $\text{La}_{1-x}\text{Sr}_x\text{MnO}_{3-\delta}$ (LSM) material based on the calculated reaction energetics and potential energy surfaces, most of these

investigations employed the orthorhombic or ideal cubic crystal structure of LSM, which is far away from the reality. As for the more active mixed ionic and electronic conductor $\text{La}_{1-x}\text{Sr}_x\text{CoO}_{3-\delta}$ (LSC), however, to the best of our knowledge, few such literatures are available, especially focused on the surface properties related to catalysis.

Exploring the electronic structure and surface stability of cathode material at different conditions is the necessary prerequisite for interpreting the interaction between oxygen and surface. In this study, we obtained the electronic and atomic structures of LaCoO_3 and $\text{La}_{1-x}\text{Sr}_x\text{CoO}_{3-\delta}$ systems using the first-principles computation method. Then the stability of three low-index surfaces ((001), (110) and (111)) with different terminations was examined by thermodynamic phase diagram analysis.¹¹⁻¹³ This will result in a much more detailed understanding of changes in the surface stability along with the two most important environmental parameters——temperature and O_2 partial pressure.

Density functional theory (DFT) with LDA or GGA schemes can give accurate ground state properties for a variety of materials.^{14,15} However, they introduce a non-physical electron self-interaction energy meanwhile.^{16,17} To a great degree, the success of them is attributable to the cancellation of the self-interaction energy between different calculations. But for those strongly correlated systems with the on-site

Coulomb and exchange interactions, such as transition metal oxides and rare-earth compounds, they will obtain poor magnetic ground state and electronic structure because the error cancellation can't be relied upon any more.¹⁸ This problem can be effectively mitigated by DFT+*U* method¹⁹ which selectively introduces an empirical Hubbard energy correction to account for the on-site Coulomb interactions in the localized electron states (d, f orbitals) whose self-interaction is particularly large. Here we adopted the GGA+*U* approach for the 3*d* electrons of Co element.

2. Computational methods

2.1 First-principles calculation details

All periodic spin polarized first-principles computations were performed using the plane-wave pseudopotential technique with the projector-augmented wave (PAW)²⁰ to model the ion-electron interaction as implemented in the Vienna ab initio simulation package (VASP).^{21,22} The generalized gradient approximation +*U* (GGA+*U*) scheme with the Perdew–Burke–Ernzerhof (PBE)^{23,24} functional and a 400 eV cutoff for the plane-wave basis set were used throughout the computations. La, Sr, Co, and O atoms were described by 11 ($5s^25p^65d^16s^2$), 10 ($4s^24p^65s^2$), 9 ($4s^13d^8$), and 6 ($2s^22p^4$) valence electrons, respectively. The atomic positions of all the structures were fully relaxed using the conjugate gradient method during the geometry

optimizations. The convergence thresholds were set as 10^{-6} eV for energy and 0.05 eV/Å for force. $4\times 4\times 4$ and $4\times 4\times 1$ Monkhorst-Pack k -point meshes²⁵ in the Brillouin zone were used for $2\times 2\times 2$ perovskite supercell containing 40 atoms and seven-layer slab geometry optimizations, respectively, so that the k -point density in reciprocal space were kept close to each other.

The rotationally invariant GGA+ U approach in the simplified spherically averaged version^{26,27} was adopted, where the parameters U and J enter into the density functional as a combined effective interaction parameter, $U_{\text{eff}}=U-J$. According to the literature,²⁸ $J=1$ eV was used in all our GGA+ U calculations. The value of U_{eff} (3.0 eV) was determined by bandgap scan of bulk LaCoO₃ material, which will be introduced in section 3.1 in detail.

Orthorhombic and cubic are the two most common phases of LaCoO₃ material. Here only the cubic phase ($Pm3m$) was considered because LaCoO₃ has a cubic structure under SOFC operating conditions above 500 °C in ambient air (the cooperative Jahn-Teller orbital order/disorder transition temperature is about 500K²⁹). And the cubic-structure Sr-doped LaCoO₃ models (bulk and slabs) were generated based on undoped LaCoO₃ systems. On the other hand, although it is on average cubic under the high-temperature conditions, the local J-T distortion persisted structure is more realistic than the ideal

one.³⁰ Therefore We have carried out calculations keeping overall cubic symmetry constraints but allowing for local distortions inside the supercell. For bulk computations, ideal cubic unit cells without internal relaxation were first performed to obtain lattice constants and then ions positions were optimized internally in a $2\times 2\times 2$ cubic supercell to restore CoO_6 octahedron rotation (Figure 2). The surfaces slab calculations were performed with lattice parameters a , b identical to those of bulk supercell while that in the c direction was relaxed freely.

Previous studies indicate that neglect of spin polarization will result in considerable errors in material properties.⁷ Thus the spin-polarized computations were carried out in this study to properly describe the magnetic property of LaCoO_3 -based materials and the triplet ground state of oxygen ($^3\text{O}_2$). It is well known that the magnetic states of perovskite materials are quite complex and undergo phase transitions at elevated temperatures. Experimental results show that LaCoO_3 is paramagnetic³¹ under the SOFC operating conditions ($T = 800\text{-}1500$ K). Different magnetic states (NM: nonmagnetic; FM: ferromagnetic; A-AFM: A type antiferromagnetic; C-AFM: C type antiferromagnetic; G-AFM: G type antiferromagnetic) of bulk LaCoO_3 system were tested here. Results indicate that the NM configuration of LaCoO_3 is the most stable magnetic state, which is in agreement with the experimental conclusion³¹.

The structures and stability of three low-index surfaces——(001), (110) and (111) with different terminations were discussed here by calculating several properties, including the atomic displacements, surface energies, electron densities, Bader charges,³²⁻³⁴ the Gibbs free energies under different external conditions, etc. The nonstoichiometric symmetrical slabs (odd number of layers, the same terminations on both sides, e.g., CoO₂ or LaO for (001) surface.) were adopted because these cancel the dipole moment³⁵ of stoichiometric nonsymmetrical ones (even number of planes, different terminations on both sides), which would reduce the computation time. In addition, this kind of model allows us to investigate separately the properties of different terminations (e.g., LaO-(001) and CoO₂-(001)), which is indispensable for thermodynamic analysis of surface stability under different conditions.

Our test results indicated that seven-layer slabs were thick enough for all three surfaces with different terminations to show convergence of the main properties, which is in line with literature.^{6,7} The periodically repeated slabs were separated by a vacuum space of 16 Å along the *z* direction in order to eliminate the interaction between the surfaces through the vacuum region.

Moreover, bulk lattice optimization and energy calculation were also performed on these metals and corresponding oxides, La, Co, Sr, La₂O₃, CoO, Co₃O₄, SrO and SrCoO₃, involved in the thermodynamic stability

investigation of $\text{La}_{1-x}\text{Sr}_x\text{CoO}_3$ low-index surfaces.

2.2 Thermodynamics principles of surface stability

The thermodynamics calculation scheme used in this work to determine the stability of different surfaces with different terminations of complicated oxides which are in equilibrium with environmental conditions (oxygen partial pressure, temperature, etc.) had been introduced in detail in literature^{8,11,12,36,37} and the references therein. It's based on the data of foregoing first-principles calculations. Here is a brief description of the analysis process (Sr-doped LaCoO_3 system, $\text{La}_{1-x_b}\text{Sr}_{x_b}\text{CoO}_3$, is taken as an example, $x_b = 0.125$).

We'll begin with the characteristics of the most stable surface: (I) it is in equilibrium with both bulk material and the surrounding oxygen atmosphere; (II) it has the lowest positive surface Gibbs free energy.

Firstly, for a certain surface of $\text{La}_{1-x_b}\text{Sr}_{x_b}\text{CoO}_3$ system, criterion (I) means that the chemical potentials of four constituents (La, Sr, Co and O) follow the well-known relationship:

$$(1 - x_b)\mu_{La} + x_b\mu_{Sr} + \mu_{Co} + 3\mu_O = \mu_{LSC}^0 = E_{bulk}^{LSC} \quad (1)$$

where μ_{LSC}^0 , μ_{La} , μ_{Sr} , μ_{Co} , μ_O and E_{bulk}^{LSC} denote the standard chemical potential of the bulk $\text{La}_{1-x_b}\text{Sr}_{x_b}\text{CoO}_3$, the chemical potentials of four constituents and the DFT energy of $\text{La}_{1-x_b}\text{Sr}_{x_b}\text{CoO}_3$ per formula unit, respectively. In Eq. (1), we substitute E_{bulk}^{LSC} for μ_{LSC}^0 , neglecting the vibrational and pV contributions because they are typically smaller than

the error of typical DFT calculation,¹¹ especially the vibrational contribution is very difficult to be calculated accurately and feasibly at present. Similar disposal had been employed in the subsequent investigations of this study. In addition, Eq. (1) also considers the strong influence of O₂ partial pressure (p_{O_2}) and temperature (T) via the variable——O chemical potential.

For our symmetrical slab models, the excess surface Gibbs free energy Ω is defined as:

$$\Omega^i = \frac{1}{A^i} [\phi_{Sr}^i - \Gamma_{Sr,Co}^i \Delta\mu_{Co} - \Gamma_{Sr,La}^i \Delta\mu_{La} - \Gamma_{Sr,O}^i \Delta\mu_O] \quad (2)$$

$$\phi_{Sr}^i = \frac{1}{2} [E_{slab}^i - N_{Sr}^i E_{bulk}^{LSC}] - \Gamma_{Sr,Co}^i E_{bulk}^{Co} - \Gamma_{Sr,La}^i E_{bulk}^{La} - \frac{1}{2} \Gamma_{Sr,O}^i E_{O_2} \quad (3)$$

$$\Gamma_{Sr,a}^i = \frac{1}{2} (N_a^i - N_{Sr}^i \frac{N_{bulk}^a}{N_{Sr}^{bulk}}) \quad (4)$$

where i denote the slab termination, e.g., $i = \text{CoO}_2$ and LaO for the (001) surface, LaCoO and O_2 for (110) surface. A^i is the surface area of i -terminated slab. E_{slab}^i, E_{bulk}^m are the DFT energies of the i -terminated slab and the bulk metal m per metal atom, respectively. $\Gamma_{Sr,a}^i$ denotes¹² the excess of component a with respect to the number of Sr ions in the i -terminated slabs. N_a^i and N_{bulk}^a are the numbers of atom a in slab and in $\text{La}_{1-xb}\text{Sr}_{xb}\text{CoO}_3$ bulk, respectively. It is obvious that ϕ^i is a constant for a certain slab. $\Delta\mu$, the chemical potential deviation of four constituents, can be calculated from Eq. (5)-(8):

$$\Delta\mu_{Co} = \mu_{Co} - E_{bulk}^{Co} \quad (5)$$

$$\Delta\mu_{Sr} = \mu_{Sr} - E_{bulk}^{Sr} \quad (6)$$

$$\Delta\mu_{La} = \mu_{La} - E_{bulk}^{La} \quad (7)$$

$$\Delta\mu_O(T, p) = \mu_O(T, p) - \frac{1}{2}E_{O_2} \quad (8)$$

According to criterion (II), excess surface Gibbs free energy (Ω) of the most stable slab i should be the positive minimum (Eq. (9), here $\Delta\mu_{Co}$ and $\Delta\mu_{La}$ are taken as independent variables), otherwise the bulk $La_{1-x_b}Sr_{x_b}CoO_3$ will disintegrate spontaneously.

$$\Omega^i(\Delta\mu_{Co}, \Delta\mu_{La}) > 0 \quad (9)$$

Eq. (10) determines the boundary between stability regions of different slabs with i and j terminations:

$$\Omega^i(\Delta\mu_{Co}, \Delta\mu_{La}) = \Omega^j(\Delta\mu_{Co}, \Delta\mu_{La}) \quad (10)$$

Besides the forbiddance of bulk's disintegrating spontaneously, the phase separation of corresponding metals (La, Sr and Co) and oxides (La_2O_3 , SrO, CoO, Co_3O_4 and $SrCoO_3$) should also be prevented to guarantee the stable existence of $La_{1-x_b}Sr_{x_b}CoO_3$ bulk and its surface, leading to the following relationships:

$$\Delta\mu_{Co} < 0 \quad (11)$$

$$\Delta\mu_{La} < 0 \quad (12)$$

$$\Delta\mu_{Sr} < 0, \text{ i.e. } (1 - x_b)\Delta\mu_{La} + \Delta\mu_{Co} + 3\Delta\mu_O > E_{LSC}^f \quad (13)$$

$$E_{La_2O_3}^f > 2\Delta\mu_{La} + 3\Delta\mu_O \quad (14)$$

$$E_{CoO}^f > \Delta\mu_{Co} + \Delta\mu_O \quad (15)$$

$$E_{Co_3O_4}^f > 3\Delta\mu_{Co} + 4\Delta\mu_O \quad (16)$$

$$E_{LSC}^f - x_b E_{SrO}^f < (1 - x_b)\Delta\mu_{La} + \Delta\mu_{Co} + (3 - x_b)\Delta\mu_O \quad (17)$$

$$\frac{1}{1-x_b} E_{LSC}^f - \frac{x_b}{1-x_b} E_{SrCoO_3}^f < \Delta\mu_{La} + \Delta\mu_{Co} + 3\Delta\mu_O < E_{LaCoO_3}^f \quad (18)$$

where E^f is the formation energy of corresponding oxide material calculated from the DFT energies.

Last but not least, in order to obtain more accurate result, the chemical potential deviation of O atom $\Delta\mu_O(T, P)$ is computed by using thermodynamics data³⁸ according to literature,^{12,13}

$$\Delta\mu_O(T, P) = \frac{1}{2} \left\{ \Delta G_{O_2}(T, p^0) + RT \ln\left(\frac{P}{p^0}\right) \right\} + \delta\mu_O^0 \quad (19)$$

$$\Delta G_{O_2}(T, p^0) = G_{O_2}(T, p^0) - G_{O_2}(T^0, p^0) \quad (20)$$

where G denotes the Gibbs free energy of O_2 , $T^0 = 298.15$ K, $p^0 = 1$ atm. $\delta\mu_O^0$, a correction term to compensate the reference state deviation of our theoretical calculations from that of experimental data, is estimated from the following Eq. (21),

$$\delta\mu_O^0 = \frac{1}{n} \sum \left\{ \frac{1}{y} (E_{M_xO_y} - xE_M - \Delta H_{M_xO_y}^{f,0}) - \frac{1}{2} (E_{O_2} + T^0 S_{O_2}^{gas}(T^0, p^0)) \right\} \quad (21)$$

here E , $\Delta H^{f,0}$, S , and n denote the DFT energies of metals, oxides and O_2 , the experimental standard formation enthalpies of metal oxides, the experimental standard entropy of O_2 , and the number of metal oxide species, respectively.

Then we can plot the phase diagrams to predict the stability of different surfaces with different terminations. The investigation on undoped $LaCoO_3$ system complies with similar process.

3. Results and discussion

3.1 Atomic and electronic structures

3.1.1 U parameter optimization and properties of bulk LaCoO_3

Before the investigation on surfaces of LSC materials, we firstly determined the value of U_{eff} for Co element, which is generally related to the valence state and the crystal structure, through examining the atomic and electronic structures of the bulk LaCoO_3 . Band gap scan calculations were performed with the U_{eff} changing from 1.1 to 6.0 eV for every 0.1 eV (Figure 1). From this graph, it is found that the band gap of bulk cubic LaCoO_3 remains closed when $U_{\text{eff}} < 2.2$ eV, while the value of the band gap increases linearly with U_{eff} on the whole after it is opened at $U_{\text{eff}} = 2.3$ eV. When $U_{\text{eff}} = 3.0$ eV is employed, a band gap of 0.31 eV is obtained, which agrees with the experimental result very well.³⁹ In addition, the effective interaction parameter $U_{\text{eff}} = 3.0$ eV is very close to the value suggested by Morgan et al.,²⁸ 3.3 eV. Thus the $U_{\text{eff}} = 3.0$ eV was used for all the subsequent GGA+ U calculations to investigate the atomic, electronic structures and phase stability of the surfaces of LSC materials.

Figure 2(a) shows the optimized $2 \times 2 \times 2$ supercell structure of undoped LaCoO_3 , local distortion could be noticed. The rotation angles of CoO_6 octahedrons around the three principle axes (x , y , z) are about $\pm 6.8^\circ$, $\pm 7.5^\circ$ and $\pm 7.5^\circ$, respectively. The Co-O bond lengths are around 1.93-1.98 angstrom. All the $\angle \text{Co-O-Co}$ and $\angle \text{O-Co-O}$ are about $159-160^\circ$, $88-92^\circ$, respectively.

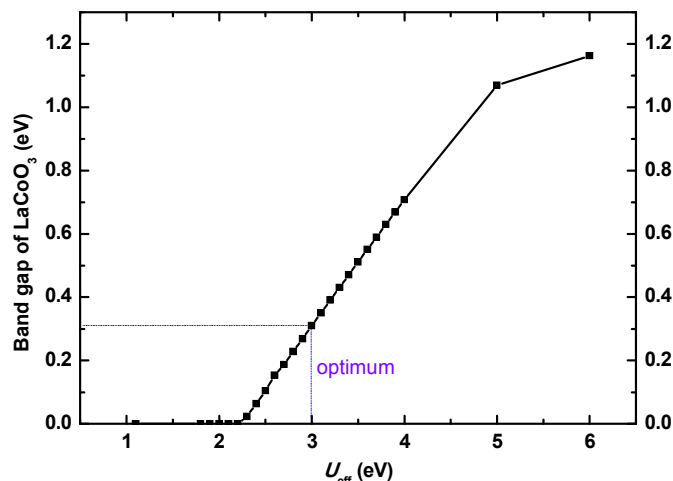


Figure 1. Band gap of cubic LaCoO₃ as a function of effective interaction parameter U_{eff} (1.1 - 6.0 eV) calculated by GGA+ U scheme.

The optimized parameters of cubic LaCoO₃ and corresponding experimental results are presented in Table 1. It is obvious that the calculated lattice constants are in good agreement with the experimental ones⁴⁰ as well as previous computational results.²⁸ As for Co³⁺, there are three possible spin states (Figure 1S), e.g. high spin (HS, $t_{2g}^4 e_g^2$), intermediate spin (IS, $t_{2g}^5 e_g^1$) and low spin (LS, $t_{2g}^6 e_g^0$). The calculated magnetic moments of Co ions in the 2×2×2 supercell, either local or average, demonstrate that Co ions adopt a mixed LS-IS state which is some different from the experimental result,⁴⁰ mixed IS-HS state, measured under the condition of high-temperature SOFC. This should be attributed to the limitation of first-principle method that it can not yet be used to calculate properties above 0 K at present.

In addition, the Bader charge of La, +2.092e, is close to its formal charge of +3e, while those of Co and O ions, +1.349e and -1.147e, are

much smaller than their formal charges of +3e, -2e. This indicates that the Co–O chemical bond presents the notable feature of covalent bonding, which is typical for ABO₃ perovskites. The electron density difference maps of LaCoO₃ system (Figure 3) confirms this conclusion.

In a word, the calculated results (lattice constants, local magnetic moments and Bader charges) of undoped LaCoO₃ bulk are consistent with experimental and other theoretical results on the whole, indicating our model and parameters are reasonable.

Table 1. Optimized lattice constants, local magnetic moments, Bader charges of 2×2×2 bulk cubic LaCoO₃ structure.

This work	$a = b = c$ (Å)		3.856
	local magnetic moment * (μ_B , per Co atom)		0.29, 1.78-2.17 (1.75)
	Spin state		LS/IS ($t_{2g}^{5+\delta} e_g^{1-\delta}$)
	Bader charge (e , averaged over all ions of the same type)	q_{La}	2.092
		q_{Co}	1.349
		q_O	-1.147
Other calculated results ²⁸	$a = b = c$ (Å)		3.848
	local magnetic moment (μ_B , per Co atom)		1.8-2.0 (2.0)
	Spin state		IS
	Bader charge (e)	q_{La}	2.083
		q_{Co}	1.501
		q_O	-1.195
Experimental data ⁴⁰	$a = b = c$ (Å)		3.85-3.90
	local magnetic moment		2-4
	Spin state		IS/HS ($t_{2g}^{5-\delta} e_g^{1+\delta}$)

* The local magnetic moments are calculated from the difference between electron density of up and down spins projected onto Wigner-Seitz sphere of Co (radius is 1.302 Å), while those in parentheses are the average values from the total magnetic moments of the 2×2×2 supercell.

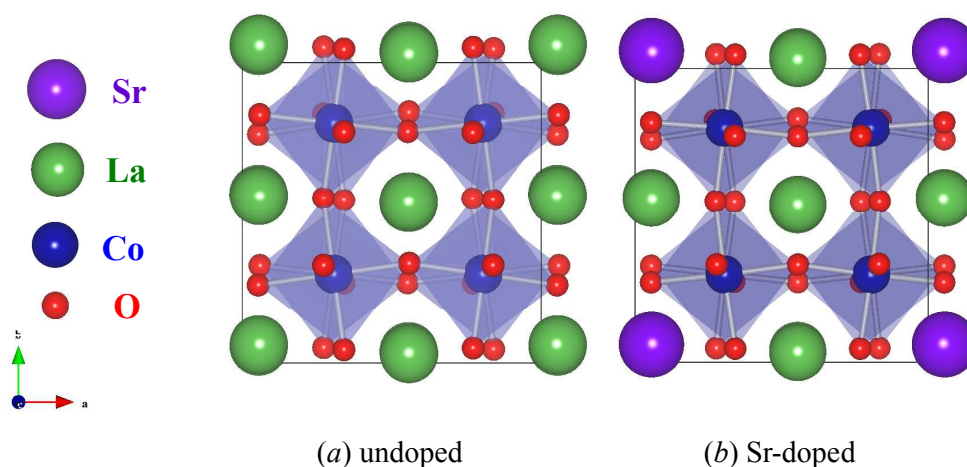


Figure 2. Optimized structures of undoped and Sr-doped LaCoO₃.

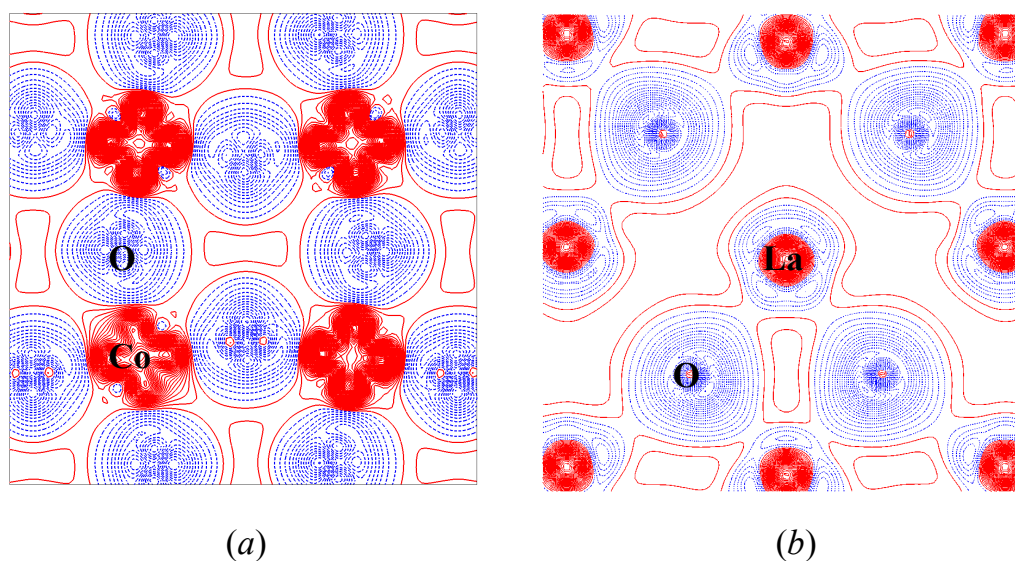


Figure 3. Electron density difference maps of the CoO₂ (a) and LaO (b) planes in bulk LaCoO₃ crystal calculated with respect to the superposition of atomic densities. Solid (red) and dash (blue) lines represent deficiency and excess of the electron charge, respectively, with the increment of 0.003 e/Å³.

3.1.2 Sr-doped cubic LaCoO₃ system——La_{0.875}Sr_{0.125}CoO₃

It's well known that the smaller the Sr content, the larger the necessary system supercell size. In order to improve the current computational study of Sr-doped system more feasible to be carried out, the model of LaCoO₃ with a 12.5% Sr doping was chose to be set up

because it is very close to typical experimental concentrations ($\leq 10\%$ Sr). In the formerly optimized $2 \times 2 \times 2$ LaCoO_3 supercell, a Sr concentration of $x = 0.125$ was achieved by replacing one of the eight La by Sr (Figure 2 (b)). The optimized parameters of Sr-doped LaCoO_3 are listed in Table S1. It can be seen that the lattice constants almost keep the same as those of undoped LaCoO_3 . The rotation angles of CoO_6 octahedrons around the three principle axes (x , y , z) are about $\pm 6.3^\circ$, $\pm 7.1^\circ$ and $\pm 7.0^\circ$, respectively. The Co-O bond lengths are around 1.94-1.97 angstrom. All the $\angle \text{Co-O-Co}$ and $\angle \text{O-Co-O}$ are about $159-163^\circ$, $88-93^\circ$, respectively.

The local magnetic moments, 1.48-1.53 μ_B , imply that Co ions in $\text{La}_{0.875}\text{Sr}_{0.125}\text{CoO}_3$ bulk also take on mixed LS-IS state. The Bader charges of La and Sr ions, +2.094 e and +1.593 e , are close to their formal charges, which is similar to the undoped LaCoO_3 . However, Bader charge of Co ion, +1.281 e , is more negative than that in undoped LaCoO_3 bulk system, +1.349 e , indicating that Sr-doping causes a decrease of the Co-O bond covalency.

3.1.3 Optimized lattice parameters of related metals and oxides

Table S2 shows the optimized lattice constants of all metals and oxides relate to the surface thermodynamic stability analysis of $\text{La}_{1-x}\text{Sr}_x\text{CoO}_3$ systems, which are all in good agreement with the experimental values.⁴¹⁻⁴⁸ In addition, the O-O bond length and

vibrational frequency of O₂ molecule we obtained are 1.23 Å and 1563 cm⁻¹, respectively, which are in good accordance with experimental results,^{49,50} 1.21 Å and 1550 cm⁻¹. All these again demonstrate the models and parameters used in this study are reasonable.

3.1.4 Low-index surfaces of undoped LaCoO₃

The relaxed configurations of three low-index surfaces of undoped LaCoO₃ system—(001), (110) and (111) with different terminations were displayed in Figure 4. Compared to the bulk-truncated surface structures, considerable reconstruction or rumpling occurred in all these slabs, especially along the *z* direction vertical to the surface planes. To describe it in detail, LaO- and CoO₂-terminated (001) surface slabs were taken as examples. The calculated atomic displacements are listed in Table 2 (the layer numbered scheme is shown in Figure S2). In the LaO-terminated (001) slab, displacements toward the slab center (0.05 - 1.35 % of bulk lattice constant) are observed for those top-layer La of both sides, whereas the La ions in other layers move in the opposite direction (0.10 - 1.18 %). All the Co and O ions in this slab go outward. The order of displacement values is: O > Co > La. In the CoO₂-terminated (001) slab, all La ions move toward the top-layer (1.44 - 2.33 %), while the cases of Co and O ions are more complicated, some go inward the slab center and others move outward, which maybe result from the tilting of the CoO₆ octahedra. For both (001) slabs, it also can be

seen that the displacements of ions decrease gradually when going along the [001] direction from top-layer to the inner-layer, whose properties are close to those of the bulk. This theoretical prediction of surface wavy distortion could be examined by means of experiments, such as LEED technique, etc.

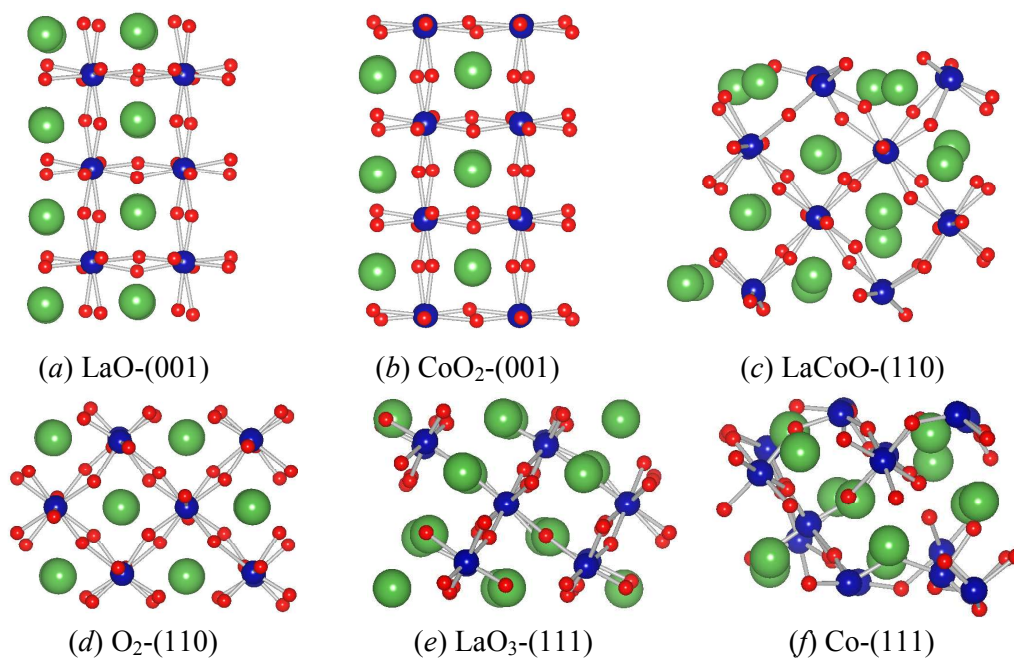


Figure 4. Side views of three low-index surfaces of cubic LaCoO₃ system with different terminations.

Table 2. Calculated atomic displacements along the z direction (in percent of bulk lattice constant, and the 4th layer is taken as the reference plane), Bader charges q_B (e) and the deviations from bulk average values Δq_B (e) of LaO- and CoO₂-terminated (001) surfaces. Negative sign of displacement means atom moving toward the slab center. 1-7 are sequence numbers of slab layers from one side to the other side (as shown in Figure S2).

Layer sequence	LaO-terminated (001)				CoO ₂ -terminated (001)			
	Atom	Displacement Δz (%)	Bader charge (e)		Atom	Displacement Δz (%)	Bader charge (e)	
			q_B	Δq_B			q_B	Δq_B
1	La	0.10, -0.05 ~ -1.35	1.98 ~ 2.02	-0.07 ~ -0.11	Co	0.42 ~ 0.74	1.43 ~ 1.46	0.08 ~ 0.11
	O	3.59 ~ 5.70	-1.28 ~ -1.34	-0.13 ~ -0.19	O	0.32 ~ 1.28, -0.06 ~ -1.23	-0.92 ~ -1.08	0.07 ~ 0.23
2	Co	1.61 ~ 2.19	1.24 ~ 1.30	-0.05 ~ -0.11	La	1.44 ~ 1.97	2.10, 2.11	0.01, 0.02
	O	1.45 ~ 3.36	-1.18 ~ -1.21	-0.03 ~ -0.07	O	0.13, -0.66 ~ -0.86	-1.12 ~ -1.16	-0.01 ~ 0.03
3	La	0.22 ~ 1.18	2.09	-0.01 ~ 0.00	Co	-0.04 ~ -0.18	1.37 ~ 1.40	0.02 ~ 0.05
	O	0.04 ~ 1.45	-1.19 ~ -1.22	-0.05 ~ -0.07	O	0.28 ~ 0.82, -0.07 ~ -0.50	-1.10 ~ -1.13	0.01 ~ 0.05
4	Co	—	1.33 ~ 1.49	-0.02 ~ 0.14	La	—	2.09, 2.10	0.00
	O	—	-1.16, -1.17	-0.01 ~ -0.03	O	—	-1.14 ~ -1.16	-0.01 ~ 0.01
5	La	0.10 ~ 1.16	2.08, 2.09	-0.01 ~ 0.00	Co	0.56 ~ 0.74	1.36 ~ 1.39	0.01 ~ 0.04
	O	0.04 ~ 1.47	-1.19, -1.21	-0.04 ~ -0.06	O	-0.02, 0.33 ~ 1.36	-1.12 ~ -1.15	0.00 ~ 0.03
6	Co	1.78 ~ 2.26	1.24 ~ 1.30	-0.05 ~ -0.11	La	2.12 ~ 2.33	2.10, 2.11	0.01, 0.02
	O	1.47 ~ 3.29	-1.18 ~ -1.20	-0.04 ~ -0.06	O	0.00 ~ 0.86	-1.13, -1.14	0.00, 0.01
7	La	-0.11 ~ -1.34	1.98 ~ 2.02	-0.07 ~ -0.12	Co	1.22 ~ 1.45	1.43 ~ 1.46	0.08 ~ 0.11
	O	3.03 ~ 3.52	-1.28 ~ -1.34	-0.13 ~ -0.19	O	0.49 ~ 2.14, -0.03 ~ -0.39	-0.91 ~ -1.08	0.07 ~ 0.24

The top-layer electron density difference maps of CoO₂-terminated (001) and LaO-terminated (001) surface slabs calculated with respect to the superposition of atomic densities are plotted in Figure S3 (a) and (b), demonstrating the considerable covalency contribution of the Co-O bonds in the top-layer, the same conclusion as that of the bulk material. In order to visualize the charge density redistribution upon surface cleavage and atomic relaxation more intuitively, we also plotted the electron density difference maps with respect to the bulk electron density in Figure 5, indicating that the surface-induced perturbation is not limited to the first layer. Electron densities of the near-surface atoms changed dramatically (considerably polarized) upon the surface formation and relaxation, while those in the inner layers changed a little or even identical to the bulk electron density (weakly perturbed). This agrees well with the conclusion of atomic displacements analysis.

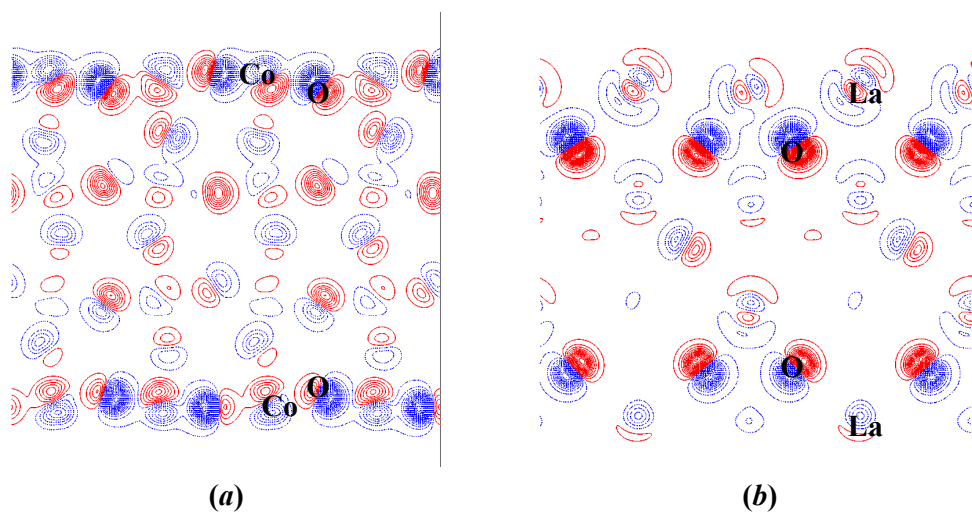


Figure 5. The electron density difference maps of CoO₂-terminated (001) (a) and LaO-terminated (001) (b) surface slabs projected to the (010) cross-sections,

calculated with respect to the bulk electron density. Solid (red) and dash (blue) lines represent deficiency and excess of the electron charge, respectively, with the increment of $0.03 e/\text{\AA}^3$.

To further elucidate the electron density redistribution, Bader charge analysis was also carried out. Bader charge q_B (e) and deviations from bulk average values Δq_B (e) of LaO- and CoO₂-terminated (001) surfaces are listed in Table 2. It is shown that the charge redistribution in the CoO₂-terminated (001) surface is restricted to the top-layer on the whole, while that of the LaO-terminated (001) surface spreads to deeper layers. The total Bader charge deviations of these two slabs with respect to the bulk are equal but have opposite signs, $\pm 3.78 e$, deviated from $\pm 4 e$, which is expected from the formal ionic charges (La³⁺, Co³⁺, O²⁻), due to the partial covalent character of Co-O bond. Furthermore, Bader charges of both Co and O ions in the CoO₂-terminated (001) slab become more positive than those in bulk, implying an increase of Co-O bond covalency near the top-layer upon the surface formation, similar conclusions were also obtained in other perovskites.¹³

Although our 7-layer slabs are nonstoichiometric, it will contain an integer number of bulk unit (LaCoO₃) as long as putting two symmetrical slabs with complementary terminations (e.g., LaO-(001) and CoO₂-(001)) together. Thus, definition of the nonstoichiometric slab surface energy is¹³

$$E_{surf} = \frac{1}{4S} (E_{t1} + E_{t2} - nE_{bulk})$$

where E_{surf} , S , E_{t1} and E_{t2} are surface energy, area of slab surface, total energies of the 7-layer slabs with complementary terminations, respectively. Energies of the corresponding structures and magnetic state in bulk LaCoO_3 crystal (nE_{bulk}) are taken as the reference level, n is the number of the bulk units. The surface energy calculation results of LaCoO_3 surfaces ((001), (110) and (111)) are summarized in Table 3.

Table 3. Calculated surface energies for the (001), (110) and (111) surfaces of undoped LaCoO_3

surface	$S (\times 10^{-19}, \text{m}^2)$	$E_{\text{surface, unrelaxed}} (\text{J/m}^2)$	$E_{\text{surface, relaxed}} (\text{J/m}^2)$
(001)LaO-term.	5.95	1.82	1.08
(001)CoO ₂ -term.	5.95		
(110)LaCoO-term.	8.41	2.79	1.66
(110)O ₂ -term.	8.41		
(111)LaO ₃ -term.	10.3	2.01	1.34
(111)Co-term.	10.3		

From the results of either unrelaxed or relaxed calculation, it can be seen that the most stable and unstable surfaces are (001), (110), respectively, among all three low-index surfaces from the point of view of the surface energy. Similar conclusion had been obtained on the investigation of LaMnO_3 material.⁵¹

3.2 Surface stability of undoped cubic LaCoO_3 system

According to the thermodynamics computation scheme described in Section 2.2, the formation energies of corresponding oxides E^f , parameters presented in the definition of the excess surface Gibbs free energy Ω and the correction term of O atom chemical potential, $\delta\mu_o^0$, had been obtained and summarized in Table S3-S5.

The formation energies of a variety of oxides calculated by GGA+ U scheme are compared with experimental formation enthalpies in Table S3. Our calculations underestimate these formation energies, which is probably induced by the + U term, contrary to the result of LaMnO₃ system⁵² calculated with GGA scheme. Fortunately, formation energy of the LaCoO₃ calculated from oxides (La₂O₃, CoO and O₂) agrees with the experimental data very well,^{53,54} which means that the errors of our calculated formation energies for oxides will cancel out one another considerably when they are used together. All these calculated formation energies of oxides are employed to plot the boundaries separating the stable LaCoO₃ area from the phases of metals and their oxides in phase diagram (Figure 6).

The right side of Figure 6 demonstrates the dependencies of the O chemical potential on the temperature and O₂ partial pressure, which were deduced from Eq. (19)-(21) using thermodynamics data.³⁸ The correction was done with the average value of $\delta\mu_o^0$ of different oxides (Table S5). The left part of Figure 6 is the surface phase diagram of LaCoO₃ drawn according to the DFT calculation results. As mentioned in Section 2.2, the most stable surface has the smallest positive excess surface Gibbs free energy. The colored areas are limited by lines where the lowest excess surface Gibbs free energy becomes zero (defined by Eq. (9)). We can tell which surface of LaCoO₃ is the most stable one under any conditions on

these grounds from Figure 6. The lines numbered from (1) to (5) in Figure 6 are the boundaries separating stable LaCoO_3 from phases of metals (La, Co) and corresponding oxides (La_2O_3 , CoO, Co_3O_4). Therefore, the LaCoO_3 material can exist stably only within the area outlined by these lines, which is prominently marked as hatched area between line 2 (precipitation of La_2O_3) and line 3 (precipitation of Co_3O_4). Five of all considered six surface slabs appear in our plotted phase diagram but only four are stable within the stability region of the cubic LaCoO_3 , qualitative description about this is summarized in Table 4.

Table 4. Qualitative description about the conditions for stable existence of the LaCoO_3 surface slabs.

Surface slabs	Conditions for stable existence (different views)		
	Chemical potential (μ)	O_2 partial pressure $p_{\text{O}_2} = 0.2 \text{ atm}$	Temperature $T = 1100 \text{ K}$
LaO-terminated (001)	low μ_{O} (O-poor limit) high μ_{Co} (Co-rich limit)	high T	low p_{O_2}
CoO ₂ -terminated (001) LaO ₃ -terminated (111)	intermediate μ_{O} intermediate μ_{Co}	Intermediate T	Intermediate p_{O_2}
O ₂ -terminated (110)	high μ_{O} (O-rich limit) low μ_{Co} (Co-poor limit)	low T	high p_{O_2}
Co-terminated (111)	Out of the hatched stability region		
LaCoO-terminated (110)	On the other side ($\Delta\mu_{\text{Co}} > 0$), unstable		

At the ambient oxygen partial pressure ($p_{\text{O}_2} = 0.2 \text{ atm}$), it is found that both CoO₂-terminated and LaO-terminated (001) surfaces can be stable in the temperature range of 750 - 1250 K, which covers the typical operational temperature of SOFC ($T = 1100 - 1200\text{K}$). Only above 1250 K, LaO-terminated (001) surface becomes dominated. CoO₂-terminated (001) and LaO₃-terminated (111) surfaces coexist between 750 K and 350

K. Then, the coexistence of three surfaces, CoO₂-terminated (001), LaO₃-terminated (111) and O₂-terminated (110), will occur from 350 K to 150 K. Next region below 150 K, the coexisting two surfaces are CoO₂-terminated (001) and O₂-terminated (110).

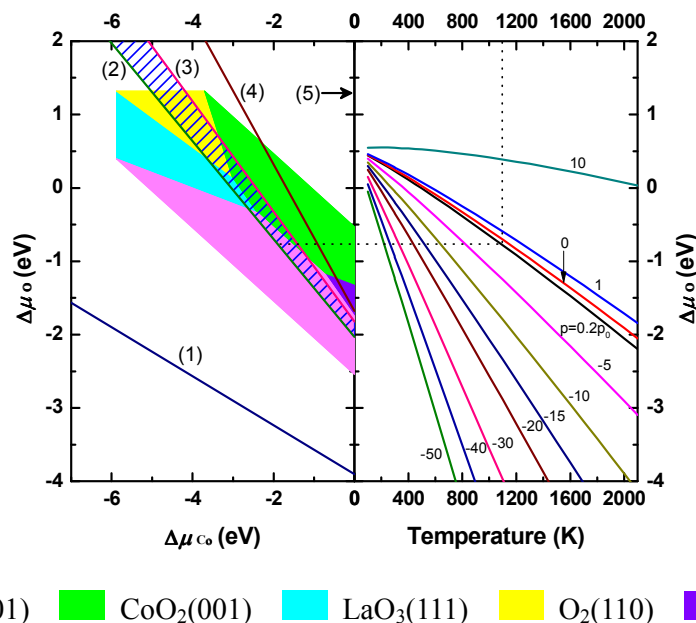


Figure 6. Phase diagram of different surfaces with different terminations in undoped LaCoO₃ system (cubic phase). The numbers in parentheses point to lines, where phase separations of metals and their oxides from bulk LaCoO₃ begin to occur: (1) La, (2) La₂O₃, (3) Co₃O₄, (4) CoO, (5) Co. Hatched area between La₂O₃ and Co₃O₄ precipitation lines represents the stable region. The right part of this figure illustrates the variance of a series of $\Delta\mu_{\text{O}}$ along with temperature and O₂ partial pressure. The labels m on the lines express the O₂ partial pressure: $p_{\text{O}_2} = 10^m$ atm.

In Figure 7, We plotted the excess surface Gibbs free energy Ω^i of all studied surfaces under the typical operational conditions of SOFC ($T = 1100$ K, $p_{\text{O}_2} = 0.2$ atm). The stability region displayed as hatched area lies between lines 2 (precipitation of La₂O₃) and 3 (precipitation of Co₃O₄). It is obvious that both LaO-terminated and CoO₂-terminated (001)

surfaces are stable in the stability region depending on the chemical potential deviation value of Cobalt, $\Delta\mu_{\text{Co}}$.

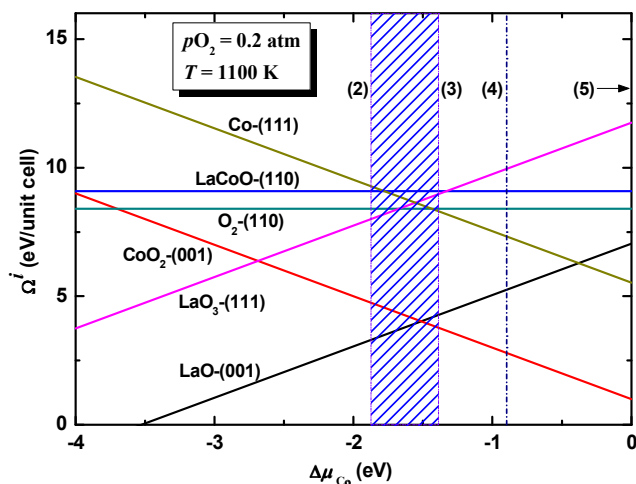


Figure 7. The variance of excess surface Gibbs free energies of all studied LaCoO_3 surfaces along with chemical potential deviation of Cobalt $\Delta\mu_{\text{Co}}$ ($T = 1100 \text{ K}$, $p\text{O}_2 = 0.2 \text{ atm}$). The numbers in parentheses point to lines are the same as those in Figure 6. Hatched area represents the stable region.

3.3 Surface stability of Sr-doped cubic LaCoO_3 system

The calculations in section 3.1.4 and 3.2 show that (001) of the LaCoO_3 crystal is the most stable surface under the typical operational conditions of SOFC. Consequently, our following studies on the Sr-doped LaCoO_3 system would only be focused on the LaO-terminated and CoO_2 -terminated (001) surface slabs, examining the influence of Sr-doping level on the stability of (001) surface slabs with two different terminations. The question needs to be answered instantly is that which LaO layer does the Sr-doping start with? Is it top-layer or central layer? It depends on the substitutional energies of Sr ion in different layers of the (001) surface slabs.

3.3.1 Sr substitutional energy

As mentioned above, the (2×2) 7-layer symmetrical models were used to estimate the Sr substitutional energies in different layers of the (001) surface slabs (Sr-doping level $x_s = 25\%$). Each (001) surface slab has two different Sr-doping configurations (LaO-terminated: 1,7- and 3,5-doping; CoO₂-terminated: 2,6- and 4-doping), as illustrated in Figure S4.

For our symmetrical models, the Sr substitutional energy is defined as follows,

$$perfect_slab + nSrO + \frac{1}{n}O_2 = defective_slab + La_2O_3 \quad (n = 1, 2)$$

$$E_{Sr,substitutional} = \frac{1}{n}(E_{defective_slab} + E_{bulk}^{La_2O_3} - E_{perfect_slab} - nE_{bulk}^{SrO} - \frac{1}{n}E_{O_2})$$

where $E_{Sr,substitutional}$, $E_{perfect_slab}$, $E_{defective_slab}$, $E_{bulk}^{La_2O_3}$, E_{bulk}^{SrO} and n are the Sr substitutional energy per Sr ion, total energies of surface slabs before and after Sr substitution, total energy of bulk La₂O₃ crystal per formula unit, total energy of bulk SrO crystal per formula unit, the number of La ions substituted by Sr ions in the surface slabs, respectively. The calculated Sr substitutional energies are presented in Table S6. Results suggest that Sr ions prefer to substitute the La ions in the outermost layers rather than those in the bulk layers for both LaO-terminated and CoO₂-terminated (001) surface slabs. The difference between Sr substitutional energies of 1,7-doping and 3,5-doping LaO-terminated (001) surface slabs, e.g. Sr segregation energy, is 0.47 eV per Sr ion, which is close to the result of

LaMnO₃ (001) surface,⁸ 0.54 eV per Sr ion.

Hence our following investigations would concentrate on the influence of Sr-doping in outermost layers on the thermodynamic stabilities of the (001) surface slabs with different terminations.

3.3.2 Phase diagrams of Sr-doped (001) surfaces

Based on the thermodynamics principles presented in section 2.2, the phase diagram for 25% outermost-layer Sr-doped (001) surfaces of La_{0.875}Sr_{0.125}CoO₃ system (Figure S4 (a) and (c)) was drawn in Figure 8, here the chemical potential deviation of O atom $\Delta\mu_o(T,P)$ was calculated under the typical operational conditions of SOFC ($T = 1100\text{K}$, $p\text{O}_2 = 0.2 \text{ atm}$).

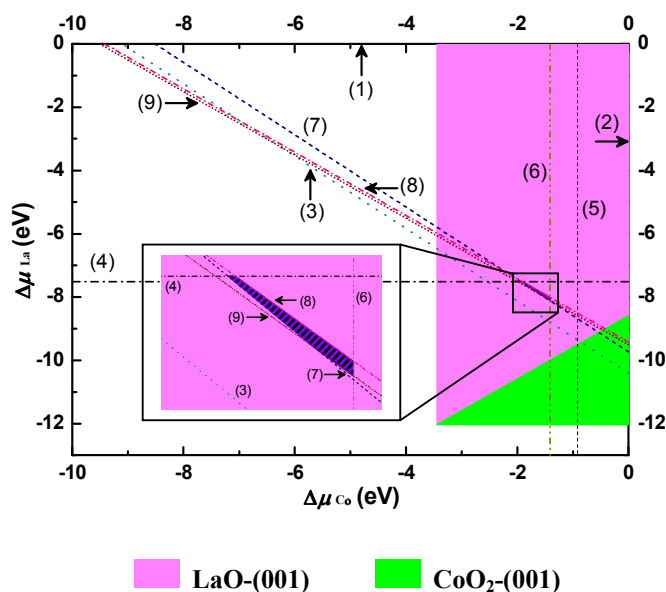


Figure 8. Phase diagram for outermost-layer Sr-doped (001) surfaces with different terminations ($x_s = 25\%$) of cubic La_{0.875}Sr_{0.125}CoO₃ system ($T = 1100\text{K}$, $p\text{O}_2 = 0.2 \text{ atm}$). The numbers in parentheses point to lines, where phase separations of metals and their oxides from bulk La_{0.875}Sr_{0.125}CoO₃ begin to occur: (1) La, (2) Co, (3) Sr, (4) La₂O₃, (5) CoO, (6) Co₃O₄, (7) SrO, (8) LaCoO₃, (9) SrCoO₃. The hatched area among La₂O₃, Co₃O₄, LaCoO₃ and SrCoO₃

precipitation lines represents the stable region. Inset shows the magnified hatched area.

It can be seen from this phase diagram that the $\text{La}_{0.875}\text{Sr}_{0.125}\text{CoO}_3$ material is stable only within small area, which means the variation ranges for both $\Delta\mu_{\text{Co}}$ and $\Delta\mu_{\text{La}}$ are narrow. Under the SOFC operational conditions, the hatched area falls in the scope of $\text{La}_{0.75}\text{Sr}_{0.25}\text{O}$ -terminated (001) surface completely, which suggests that the surface of stable $\text{La}_{0.875}\text{Sr}_{0.125}\text{CoO}_3$ crystal is not CoO_2 -terminated but $\text{La}_{0.75}\text{Sr}_{0.25}\text{O}$ -terminated. It's different from the conclusion of undoped LaCoO_3 system. In other words, Sr-doping in LaCoO_3 crystal destabilizes the CoO_2 -terminated surface with respect to the $\text{La}_{0.75}\text{Sr}_{0.25}\text{O}$ -terminated surface.

In addition, (001) surface slabs with higher level of Sr-doping in the outermost-layer (50%, 75%, 100%, models are shown in Figure S5) had also been examined to explore the influence of Sr segregation (Section 3.3.1) on the surface stability. All calculated phase diagrams are demonstrated in Figure S6. When the Sr-doping level is 50%, the same conclusion as 25% Sr-doping is obtained (Figure S6 (a)). However, if the Sr-doping level reaches to 75% and above, as illustrated in Figure S6 (b) and (c), both the $\text{La}_{0.75}\text{Sr}_{0.25}\text{O}$ -terminated and the CoO_2 -terminated (001) surface slabs become unstable, which probably results from the strong repulsion among the enriched Sr ions in the outermost LaSrO layers.

4. Conclusions

In this study, we investigated the atomic, electronic structures and the thermodynamic stability of LaCoO_3 low-index surfaces using spin-polarized GGA+ U calculations. Ferromagnetic nonstoichiometric symmetrical slab models were employed. Sr segregation on the outermost layers and the influence of Sr-doping on the thermodynamic stability of the surfaces were also examined. The main conclusions are as follows:

- (1) Through bandgap scan of bulk LaCoO_3 material, the U_{eff} used in GGA+ U calculations was determined as 3.0 eV, which is very close to literature's data.
- (2) Results of electron density difference and Bader charge analysis suggest the considerable covalency contribution of the Co-O bonds in both the bulk materials and the surface slabs. Covalency contribution increase of Co-O bonds in the CoO_2 -terminated (001) surface was observed upon the surface formation.
- (3) In undoped LaCoO_3 system, the thermodynamic phase diagram analysis demonstrates that CoO_2 - and LaO-terminated (001) surfaces are the most stable two of all considered surfaces under typical operational conditions of the solid oxide fuel cells ($T = 1100$ K, $p_{\text{O}_2} = 0.2$ atm).
- (4) Sr ions prefer to substitute La ions in the outermost layers rather than those in bulk layers for both (001) surfaces. Sr-doping destabilizes

the CoO_2 -terminated surface with respect to the $\text{La}_{0.75}\text{Sr}_{0.25}\text{O}$ -terminated surface.

These detailed results of $\text{La}_{1-x}\text{Sr}_x\text{CoO}_3$ surface properties at the atomistic level are of high importance for the further study of the oxygen reduction mechanism at the $\text{La}_{1-x}\text{Sr}_x\text{CoO}_3$ cathode.

Acknowledgements

We acknowledge the computational resources provided by the Center for Research Computing at the University of Notre Dame. Financial supports for this work were provided by the National Science Foundation-GAOLI Project under Contract No. CBET 09-67434, Shandong Provincial Natural Science Foundation (China, No. ZR2012BQ010) and the Scientific Research Foundation for the Returned Overseas Chinese Scholars (State Education Ministry of China). The authors are also greatly indebted to Prof. William F. Schneider and Mr. Mike Penninger in University of Notre Dame for many stimulating discussions on the first principles calculations and the model construction.

Notes and References

- 1 B. C. H. Steele and A. Heinzl, *Nature*, 2001, **414**, 345.
- 2 C. Xia and M. Liu, *Adv. Mater.*, 2002, **14**, 521.
- 3 L. Wang, R. Merkle and J. Maier, *J. Electrochem. Soc.*, 2010, **157**, B1802.
- 4 W. Zhou, R. Ran and Z. Shao, *J. Power Sources*, 2009, **192**, 231.

- 5 X. Lu, P. W. Faguy and M. Liu, *J. Electrochem. Soc.*, 2002, **149**, A1293.
- 6 E. A. Kotomin, Y. A. Mastrikov, E. Heifets and J. Maier, *Phys. Chem. Chem. Phys.*, 2008, **10**, 4644.
- 7 Y. A. Mastrikov, R. Merkle, E. Heifets, E. A. Kotomin and J. Maier, *J. Phys. Chem. C*, 2010, **114**, 3017.
- 8 S. Piskunov, E. Heifets, T. Jacob, E. A. Kotomin, D. E. Ellis and E. Spohr, *Phys. Rev. B*, 2008, **78**, R121406.
- 9 Y. Choi, M. C. Lin and M. Liu, *Angew. Chem, Int. Ed.*, 2007, **46**, 7214.
- 10 Y. Choi, M. E. Lynch, M. C. Lin and M. Liu, *J. Phys. Chem. C*, 2009, **113**, 7290.
- 11 K. Reuter and M. Scheffler, *Phys. Rev. B*, 2001, **65**, 035406.
- 12 K. Johnston, M. R. Castell, A. T. Paxton and M. W. Finnis, *Phys. Rev. B*, 2004, **70**, 085415.
- 13 E. Heifets, S. Piskunov, E. A. Kotomin, Y. F. Zhukovskii and D. E. Ellis, *Phys. Rev. B*, 2007, **75**, 115417.
- 14 G. Ceder, G. Hautier, A. Jain and S. P. Ong, *MRS Bull.*, 2011, **36**, 185.
- 15 K. Kang, Y. S. Meng, J. Bréger, C. P. Grey and G. Ceder, *Science*, 2006, **311**, 977.
- 16 A. Rohrbach, J. Hafner and G. Kresse, *J. Phys. Condens. Matter*, 2003, **15**, 979.
- 17 J. Heyd, J. E. Peralta, G. E. Scuseria and R. L. Martin, *J. Chem. Phys.*, 2005, **123**, 174101.
- 18 V. I. Anisimov, F. Aryasetiawan and A. I. Lichtenstein, *J. Phys. Condens. Matter*, 1997, **9**, 767.
- 19 V. I. Anisimov, J. Zaanen and O. K. Andersen, *Phys. Rev. B*, 1991, **44**, 943.
- 20 P. E. Blöchl, *Phys. Rev. B*, 1994, **50**, 17953.
- 21 G. Kresse and J. Hafner, *Phys. Rev. B*, 1993, **47**, 558.
- 22 G. Kresse and J. Furthmüller, *Phys. Rev. B*, 1996, **54**, 11169.
- 23 J. P. Perdew and Y. Wang, *Phys. Rev. B*, 1992, **45**, 13244.
- 24 J. P. Perdew, J. A. Chevary, S. H. Vosko, K. A. Jackson, M. R. Pederson, D. J. Singh and C. Fiolhais, *Phys. Rev. B*, 1992, **46**, 6671.
- 25 H. J. Monkhorst and J. D. Pack, *Phys. Rev. B*, 1976, **13**, 5188.
- 26 A. I. Lichtenstein, V. I. Anisimov and J. Zaanen, *Phys. Rev. B*, 1995, **52**, R5467.
- 27 S. L. Dudarev, G. A. Botton, S. Y. Savrasov, C. J. Humphreys and A. P. Sutton, *Phys. Rev. B*, 1998, **57**, 1505.
- 28 Y.-L. Lee, J. Kleis, J. Rossmeisl and D. Morgan, *Phys. Rev. B*, 2009, **80**, 224101.
- 29 C. Zobel, M. Kriener, D. Bruns, J. Baier, M. Gruninger, T. Lorenz, P. Reutler and A. Revcolevschi, *Phys. Rev. B*, 2002, **66**, R020402.
- 30 M. C. Sanchez, G. Subias, J. Garcia and J. Blasco, *Phys. Rev. Lett.*, 2003, **90**, 045503.
- 31 J. B. Goodenough and P. M. Racciah, *J. Appl. Phys.*, 1965, **36**, 1031.
- 32 R. F. W. Bader, *Atoms in Molecules - A Quantum Theory*. Clarendon Press: Oxford, 1994.
- 33 G. Henkelman, A. Arnaldsson and H. Jónsson, *Comput. Mater. Sci.*, 2006, **36**, 354.
- 34 <http://theory.cm.utexas.edu/bader/>.
- 35 C. Noguera, *Physics and Chemistry of Oxide Surfaces*. Cambridge University Press: New York, 1996.
- 36 I. Batyrev, A. Alavi and M. W. Finnis, *Faraday Discuss.*, 1999, **114**, 33.
- 37 F. Bottin, F. Finocchi and C. Noguera, *Phys. Rev. B*, 2003, **68**, 035418.
- 38 M. W. Chase, *NIST-JANAF Thermochemical Tables*. American Chemical Society, Washington DC, 1998.

- 39 T. Arima, Y. Tokura and J. B. Torrance, *Phys. Rev. B*, 1993, **48**, 17006.
- 40 P. M. Raccach and J. B. Goodenough, *Phys. Rev.*, 1967, **155**, 932.
- 41 A. Taylor and R. W. Floyd, *Acta Crystallographica*, 1950, **3**, 285.
- 42 J. J. Hanak and A. H. Daane, *Acta Crystallographica*, 1956, **9**, 559.
- 43 E. A. Sheldon and A. J. King, *Acta Crystallographica*, 1953, **6**, 100.
- 44 X. Liu and C. T. Prewitt, *Physics and Chemistry of Minerals*, 1990, **17**, 168.
- 45 S. Sasaki, K. Fujino and Y. Takeuchi, *Proceedings of the Japan Academy*, 1979, **55**, 43.
- 46 P. Aldebert and J. P. Traverse, *Materials Research Bulletin*, 1979, **14**, 303.
- 47 D. Taylor, *Transactions of the British Ceramic Society*, 1984, **83**, 5.
- 48 P. Bezdicka, A. Wattiaux, J. C. Grenier, M. Pouchard and P. Hagemuller, *Zeitschrift fuer Anorganische und Allgemeine Chemie*, 1993, **619**, 7.
- 49 *NIST Computational Chemistry Comparison and Benchmark Database*, 14th ed. American Chemical Society: Washington DC, 2006.
- 50 G. Herzberg, *Molecular Spectra and Molecular Structure: Volume I - Spectra of Diatomic Molecules*, 2nd ed. Krieger Publishing Company: Malabar, FL, 1950.
- 51 Y. Choi, D. S. Mebane, M. C. Lin and M. Liu, *Chem. Mater.*, 2007, **19**, 1690.
- 52 Y. A. Mastrikov, E. Heifets, E. A. Kotomin and J. Maier, *Surf. Sci.*, 2009, **603**, 326.
- 53 S. Stølen, F. Grønvold, H. Brinks, T. Atake and H. Mori, *J. Chem. Thermodynamics*, 1998, **30**, 365.
- 54 J. H. Cheng, A. Navrotsky, X. D. Zhou and H. U. Anderson, *J. Mater. Res.*, 2005, **20(1)**, 191.